applied sciences

MDPI

Article

In-Vitro Simulation of the Blood Flow in an Axisymmetric Abdominal Aortic Aneurysm

Stefania Espa *, Monica Moroni and Maria Antonietta Boniforti

DICEA-Sapienza University of Rome, via Eudossiana 18, 00184 Rome, Italy; monica.moroni@uniroma1.it (M.M.); antonietta.boniforti@uniroma1.it (M.A.B.)

* Correspondence: stefania.espa@uniroma1.it; Tel.: +39-0644585044

Received: 18 September 2019; Accepted: 24 October 2019; Published: 27 October 2019

Featured Application: To build an in-vitro physiological model, which, gaining insights from the distinctive features of the advanced image analysis technique employed for kinematic data retrieval, turns out to be suitable to investigate the correlation of the local hemodynamic characteristics (velocity and vorticity distributions, pressure and WSS fields, and, eventually, turbulence) with both the abdominal aortic aneurysm (AAA) progression and the rupture location. The perspective of this research is to build an ad-hoc methodology suitable to provide an accurate spatio-temporal measure of the WSS distribution and evolution during the cardiac cycle and correlate it with intra-luminal thrombus (ILT) deposition and possibly with rupture events.

Abstract: We investigated the blood flow patterns and the hemodynamics associated with an abdominal aortic aneurysm detected in an in vitro measurement campaign performed in a laboratory model of an aneurysm with rigid walls and an axisymmetric shape. Experiments were run in steady flow conditions and by varying the Reynolds number in the range $410 < Re < 2650$. High spatial and temporal resolution 2D optical measurements of the velocity field were obtained through a particle tracking technique known as Hybrid Lagrangian Particle Tracking. Conversely to classical Particle Image Velocimetry, both the fluid particle trajectories and the instantaneous and time-averaged velocity fields are provided without constraints on the grid size and very close to the vessel boundary. All the most relevant quantities needed to investigate the flow features were evaluated, and in particular, we focused on the wall shear stress distribution both in the healthy aortic portion and within the aneurysm. Results show that the recirculation zone in correspondence of the cavity moves downstream, and this displacement is found to increase with *Re*. Very low wall shear stress values are recovered in correspondence of the aneurysmal cavity, while a sharp peak occurs in correspondence of the reattachment point. In agreement with the literature data, the peak value is found to decrease with *Re* and to be about equal to twice the upstream value.

Keywords: blood flow; hemodynamics; image analysis; flow measurements

1. Introduction

An abdominal aortic aneurysm (AAA) is a localized irreversible dilatation of the abdominal segment of the aorta, often due to a weakening of the wall of the vessel. An AAA refers to a diameter increase of at least 50% compared to the normal arteria, which measures indicatively 2 cm. Thus, a segment of the abdominal aorta in which the diameter is equal or greater than 3.0 cm is generally considered an aortic aneurysm [1]. In developed countries, an AAA rupture represents an important cause of death with a mortality rate of approximatively 80–90% [2]; several risk factors are associated with the development of AAA including advanced age, male sex, Caucasian race, positive family history, smoking, presence of other large vessel aneurysms, and atherosclerosis [3–6].

Despite the clinical importance of AAAs, the etiology and the involved pathogenesis remain still, in part, unclear; it is, then, evident how the identification of the factors that can influence the growth and progression of the aneurysm is fundamental for Public Health management. For asymptomatic patients, repair of the aneurysm is the most effective treatment to prevent rupture but considering the risks associated with surgery, AAA repair is recommended if the risk of rupture exceeds the risks associated with surgery, which typically occurs when the AAA diameter exceeds 5.5 cm [1]. Although AAA diameter is an important predictor of rupture, not all large AAAs break, it is then fundamental to look at this phenomenon in a more complex framework. To this aim, clinical, experimental, and numerical studies are being widely performed, focusing on the deep investigation of AAAs and the determination of possible risk factors, as well as on reproducing their hemodynamics. Usually, the local hemodynamics is quantified in terms of the distributions of wall pressure, wall shear stress (WSS), and wall shear stress gradient (WSSG). The peak WSS (PWSS) and the peak wall rupture risk (PWRR) have proved to be better predictors of rupture than the maximum AAA diameter ([7] and reference therein, [8]).

The blood flow patterns associated with an AAA have been widely investigated via numerical methods [9–11]. The models may consider different levels of complexity. In [9], the authors investigated the flow field in an axisymmetric two-aneurysm model with rigid walls and assuming the blood as a Newtonian incompressible fluid in stationary conditions and in a range of Reynolds numbers $10 < Re < 2265$; the flow was characterized in terms of the distributions of wall pressure, wall shear stress (WSS) and wall shear stress gradient (WSSG). In [10] the role of the shape and of the geometric features, as asymmetry and iliac bifurcation, are investigated; in [11] the correlation between blood flow and platelet deposition mechanisms in an axisymmetric aneurysm with rigid walls was investigated in the range $300 < Re < 3600$, i.e., under both laminar and turbulent flow conditions. The numerical simulations performed using a computational fluid dynamics (CFD) package, were validated through digital particle image velocimetry (PIV) flow measurements that allowed correlating the flow pattern with the platelet deposition mechanism.

As a matter of fact, intra-luminal thrombus (ILT) has been associated with an increased rupture risk as it impacts both the biochemical and the mechanical properties of the vessel's wall in correspondence of the aneurysm [12]. In [13], the authors found that both increased ILT thickness and percentage volume are associated with AAA rupture of small aneurysms with low wall stress. In this sense, ILT may represent *a surrogate marker* of aortic wall degeneration and help in discerning high-risk aneurysms. By analyzing a large set of 'small', 'large' ruptured, and non-ruptured AAAs, they were also able to show that early AAA rupture is not a result of elevated wall stresses but the result of compromised aortic wall strength. Similar findings were obtained by Boyd et al. [14]; in this case, the authors numerically simulated the blood flow in ruptured AAAs to correlate local hemodynamic factors with rupture location.

Nevertheless, it has to be noticed that numerical study may lack of an experimental validation; to this aim, in vitro modeling [15–17] have been very useful in the characterization of the complexity implicit in cardiovascular models. In this context, Salsac et al. [18] performed flow measurements using 2D particle image velocimetry (PIV) in a rigid and symmetric model of an AAA under pulsatile flow conditions. They investigated the flow pattern and the WSS and WSSG distributions changing the geometric parameters systematically. Stamatopoulos et al. [19] studied both steady and periodic flows in an axisymmetric model of a fusiform aneurism using both computational fluid dynamics (CFD) and 2D PIV measurements in the range $100 < Re < 700$. In [20], the authors considered a rigid diseased phantom emulating the pulsatile flow in an AAA with aorto-iliac bifurcation and stenosis and measured the flow using 2D PIV. They investigated the vorticity field evolution, the vortex core trajectory, and the hemodynamics characteristics.

A now widely diffused approach consists in investigating the blood flow by combining experimental and CFD models built on patient-specific anatomical data acquired by medical imaging. Boutsianis et al. [21] used computed tomography to build a silicone model of a patient-specific AAA.

The authors measured the 3D velocity field using particle tracking velocimetry (PTV) and performed CFD simulations of the flow within the entire abdominal aorta under averaged steady physiological flow conditions and with identical boundary conditions. Stamatopoulos et al. [22] studied both steady and periodic flows in an axisymmetric model of a fusiform aneurism using both numerical simulations and laboratory experiments. In the in-vitro model, the velocity field was measured using 2D PIV, while simulations were conducted using CFD. Soudah et al. [23] used CFD on models created by 3D reconstruction of in vivo acquired computed tomography images and investigated the correlation between geometric parameters, WSS, ILT, and AAA possible rupture.

In the present study, we show the results of an in vitro measurement campaign performed in a laboratory model of the abdominal aortic segment affected by an axisymmetric AAA. We considered a simplified model of the vessel with rigid walls and symmetric shape and performed the experiments in steady flow conditions, varying the Reynolds number in the range $410 < Re < 2650$. A characterization of the flow patterns, as well as 2D measurements of the velocity field, were obtained through image analysis; in particular we used hybrid Lagrangian particle tracking (HLPT), a technique that provides both the Lagrangian (fluid particles trajectories) and the Eulerian (instantaneous and time-averaged velocity field on a regular grid) descriptions of the flow field [24]. Once the flow field is obtained, the distribution of the WSS is computed as a function of Re both in the healthy aortic portion and within the aneurism. Remarkably, particle tracking techniques compared to PIV algorithms allow a larger spatial resolution (being able to detect regions very close to the walls) and an increased dynamic range. These two features make the employment of HLPT in this context particularly suited for the computation of WSS.

The general aim of this work is to build an in vitro physiological model, which, gaining insights from the distinctive features of the advanced image analysis technique employed for image processing, is suitable to investigate the correlation of the local hemodynamic characteristics (velocity and vorticity distributions, pressure and WSS fields, and, eventually, turbulence) with both the AAA progression and the rupture location. The future perspective of this research is to build an ad-hoc methodology suitable to provide an accurate spatio-temporal measure of the WSS distribution and evolution during the cardiac cycle and correlate it with ILT deposition and possibly with rupture events.

The paper is organized as follows: In Section 2, the experimental model and the image analysis technique used to measure the velocity fields are described; in Section 3, the results concerning the flow patterns and the WSS distributions for the different Re are presented and discussed; in Section 4, the main conclusions are summarized, and some ideas for future research are outlined.

2. Materials and Methods

2.1. Design of the Experimental Model

Figure 1 shows a scheme of the experimental facility: the hydraulic loop is fed by a tank located on top of the test section. The tank is equipped with an overflow device that separates the fluid exceeding a defined level, thus ensuring a constant flow rate within the circuit. From the bottom of this tank, the fluid enters a handcrafted Pyrex tube characterized by a circular constant section of diameter $d = 1.8$ cm, modeling the healthy aorta, followed by an axisymmetric bulge, modeling the AAA (vessel model); the total length of the pipe is 140 cm.

The AAA geometry is shown in Figure 2: we considered an axisymmetric aneurysm with a dilatation ratio $D/d = 1.66$ and elongation ratio $L_a/d = 3.66$, where $D = 3$ cm and $L_a = 6.6$cm are the maximum diameter and the length of the aneurysm, respectively. Given the considered aspect ratio, we assumed that the used geometry is representative of fusiform aneurisms at a consolidated stage of the disease (i.e., increase in diameter >50%).

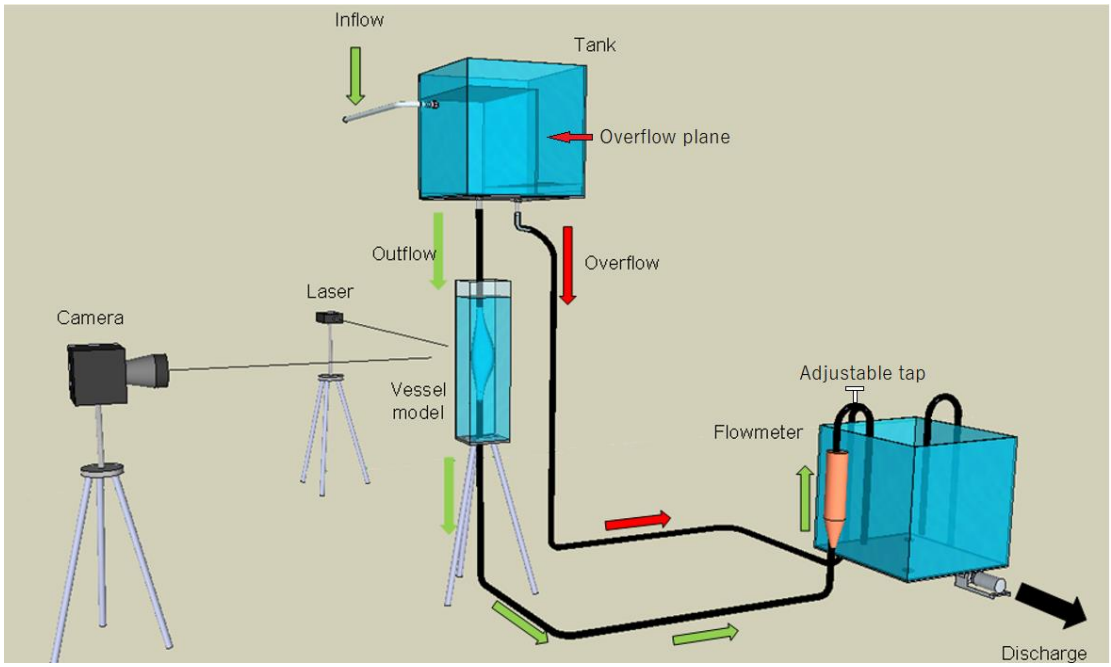

Figure 1. Experimental set-up.

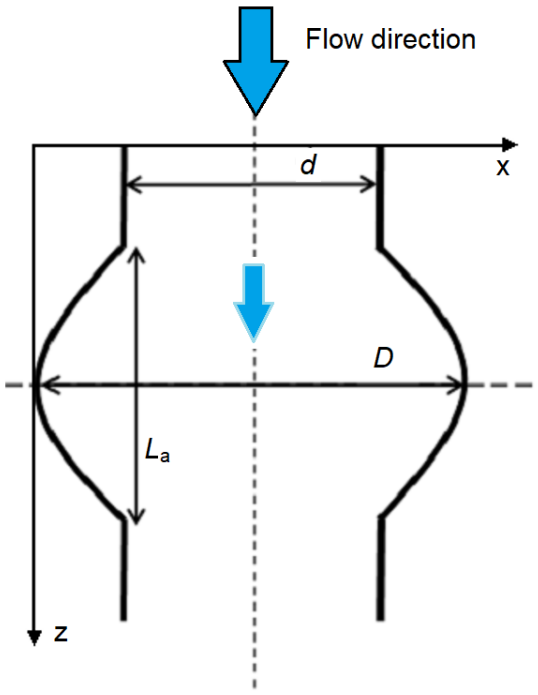

Figure 2. Geometry of the aneurysm model.

The test section consists of a portion of the tube in correspondence of the AAA enclosed in a rectangular transparent Plexiglas box 10 L × 10 W × 25 H cm^3 in order to reduce distortion. The box was filled with distilled water in which the refractive index is close to that of Plexiglas. Furthermore, the use of distilled water allows for overcoming the formation of air bubbles that may form when tap water is used. As the model aorta is made of glass, it cannot account for vessel compliance; however, it is widely accepted [22,25] that this assumption does not change the general flow characteristics. In fact, including compliance in the model only implies a slight modification in the magnitude of shear

stresses [25–28]. Also, wall rigidity can be related to vessel stiffening, which then makes it possible to model further diseases related to the presence of an aneurysm.

The working fluid is water; thus, we assumed the blood to follow in a Newtonian behavior; this assumption is compatible with the phenomena studied in this context as the vessel diameter is greater than 1 mm [18]. To fulfill geometric similarity, we considered a physiological shape of the bulge model with a 1:1 scale. As for dynamical similarity, the Reynolds number $Re = Wb\ D/\nu$ (where W_b is the bulk velocity $W_b = 4\ Q/(\pi D)^2$, Q the flow rate and ν the kinematic viscosity of the fluid) was varied in the range $410 < Re < 2650$. This range was selected according to the values corresponding to the different phases of the cardiac systole-diastole cycle; since experiments were run in steady flow conditions, the flow pattern was investigated in correspondence of the minimum, average, and peak values of Re typically observed [18]. Several experiments were performed by varying Q and for the same Q by varying the dimension of the framed area. The flow rate was tuned by an adjustable tap, and a flowmeter downstream of the test section, right before water was discharged into the outflow tank, allowed for its measure. For each experiment, the flow rate value measured by means of the flowmeter was compared with the corresponding value obtained by integrating over the cross section the velocity profile in the healthy aorta reconstructed with the image analysis algorithm described in Section 2.2. A fine agreement between the two values was recovered. The values of the main experimental parameters for each run are reported in Table 1.

Table 1. Experimental parameters in the performed experiments: spatial resolution *pixel/cm*, image acquisition frame rate *fps*, flow rate Q, bulk velocity W_b, Reynolds number Re, maximum longitudinal velocity in the healthy aorta W_m.

ID	*pixel/cm*	*fps*	Q (m^3s^{-1}) $\times 10^{-3}$	W_b (ms^{-1})	Re	W_m (ms^{-1})
1-1′	64–96	100	0.006	2.3×10^{-2}	410	4.56×10^{-2}
2-2′	64–96	100	0.009	3.3×10^{-2}	600	6.68×10^{-2}
3-3′	64–96	150	0.016	6.2×10^{-2}	1100	1.25×10^{-1}
4-4′	64–96	200	0.023	8.9×10^{-2}	1600	1.73×10^{-1}
5-5′	64–96	250	0.028	11.1×10^{-2}	2000	2.03×10^{-1}
6-6′	64–96	400	0.037	14.7×10^{-2}	2650	2.38×10^{-1}

2.2. Flow Measurements

Flow measurements were performed in the symmetric vertical mid-plane of the model test section illuminated by a diode-pumped all-solid-state 5W green laser (λ = 532 nm). This laser emits a planar sheet of 1.5mm thickness, and the distance of the test section from it was set so to obtain a uniform light distribution in the measuring section. The working fluid was seeded with a reflecting neutrally buoyant passive tracer (VESTOSINT®2157 Evonik Corporation, Germany, average diameter d_p = 56 µm, and density ρ_p = 1016 Kg/m^3), and flow images were acquired by the acquisition system, i.e., a high-speed (up to 500 fps) and high-resolution (1280 × 1024) Mikrotron EoSens camera connected to a digital video recorder IO Industries DVR Express®Core (IO Industries, Ontario, Canada).

In the first set of experiments (ID 1 to 6, see Table 1), the vertical dimension of the area framed by the camera was 20 cm and enclosed the aneurysm and a portion of healthy aorta ~12 cm long upstream of the AAA (spatial resolution of 64 px/cm). A second set of experiments was performed with the same set of parameters but increasing the spatial resolution (ID 1′ to 6′, see Table 1). In this case, the vertical dimension was 12 cm with a portion of healthy aorta ~3 cm long upstream of the AAA (spatial resolution of 96 px/cm). This set of experiments was aimed at improving the spatial resolution close to the AAA boundary to ensure a better evaluation of the WSS. The acquisition frame rate considered for each run is reported in Table 1. The maximum average displacements were on the order of 3 pixels and of 4 pixels for the first and second set of experiments, respectively.

The acquired images were processed using hybrid Lagrangian particle tracking (HLPT). The tracking algorithm is based on the solution of the optical flow equation. It selects, within each image, areas where strong light intensity gradients exist [29]; such regions can be associated with tracer particles and can then be considered as good features to track in the sequence [24]. Once the features have been identified, the algorithm reconstructs the trajectories: the fluid motion is then described in a Lagrangian frame of reference, and the velocity of the particles is evaluated by calculating the displacement along the trajectory and the corresponding elapsed time.

Image processing is achieved in three subsequent steps: 1) a pre-processing step aimed at removing the background and improving image contrast; 2) particle detection and temporal tracking via the solution of the optical flow equation to isolate particles and track them in consecutive frames; 3) post-processing to obtain the relevant flow parameters [30]. Pre-processing is carried out to improve the quality of acquired images; basically, it implies the removal of parts of the image, which are not significant for the flow analysis as the areas outside of the vessel walls. In this case, in fact, the glares due to the interaction between the laser sheet and the walls may interfere in the selection of good features by the processing algorithm. To properly border the domain, we employed a mask obtained by identifying the Cartesian coordinates of a large number of points belonging to the walls of the aneurysmal bulge and interpolating them by sixth-order polynomials. The definition of the boundaries plays a crucial role in the WSS calculation as it allows for the calculation of the unit tangent and normal vectors in correspondence of the wall (see the Appendix A).

The particle detection algorithm, the core of the HLPT technique, is based on the solution of the optical flow equation [24]: a set of positions associated with the displacement vector predictor, for which the optimization problem is well-posed, is detected via the solution of the image intensity conservation equation. Those positions, also defined as features, are then associated with the centroid coordinates using two 1D Gaussian functions built around the integer position of the local maximum of the intensity value of each detected feature. The set of validated particle image locations and the displacement vector predictor, associated with the particle, given by the approximated solution of the optical flow equation, are, finally, used as input data for the tracking algorithm.

The nearest neighbor principle is employed to identify the successive positions of each particle/feature and extract the displacement of the particle along its trajectory. Among all the possible candidates, the principle selects the one associated with the minimum Euclidean distance from the position determined with the displacement predictor. As the solution of the assignment problem is strengthened by using the displacement vector predictor, the proposed method does not suffer from the typical drawbacks of the classical nearest neighbor method, i.e., being erroneously influenced by fast-moving particles with respect to the mean inter-particle distance.

An example of reconstructed trajectories for run 6 is reported in Figure 3. The adaptive Gaussian arithmetic average method described in [30] was employed to map randomly spaced Lagrangian data onto the regular grid. After reaching the constant flow condition, properly checked through the flowmeter, each experiment lasted on average 60 s; given the characteristic time scales of the flow ~0.05 s, we estimated such a duration suitable to provide enough data to ensure a robust statistical analysis. The instantaneous flow fields are then averaged, and the time average (U, W) of both the horizontal and vertical velocity components are obtained; for all the performed measurements, we estimated fluctuations were increasing with Re of the order of (but less than) 10%. The post-processing of the velocity fields allows the calculation of all the quantities of interest for the description of the fluid motion; as it will be widely discussed in the next section, we will focus on stream function and WSS.

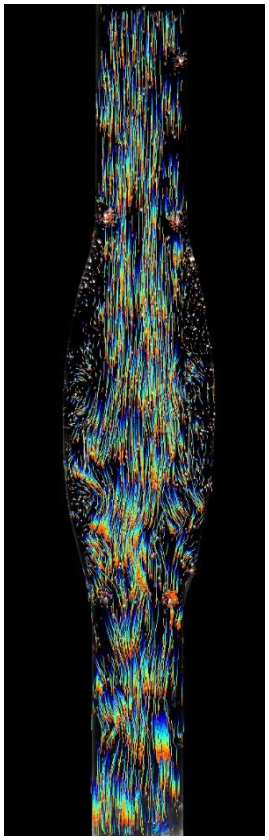

Figure 3. Example of reconstructed trajectories, run 6.

3. Results and Discussion

The velocity profiles for the whole set of experiments are shown in Figure 4. These profiles refer to both the healthy aorta and the aneurysmatic dilatation in correspondence with its maximum diameter (section AA' of Figure 2); the analytical Poiseuille profile is plotted as well; we recall that when a velocity profile follows the parabolic law, the average velocity is known to be twice the maximum velocity. Profiles have been normalized by the maximum velocity measured in the healthy aorta, W_m.

In the healthy aorta, the agreement between the measured and the parabolic profiles is quite good for $Re \leq 1100$ (cases 1, 2, 3); for $Re \geq 1600$, the difference among these two curves increases with Re. This trend was expected since the entry length l_e required for the flow to develop is a function of Re; as stated by the expression $l_e = 0.056 \times Re \times D$ proposed for axial pipe laminar flows [31]. Considering the length of the tube before the bulge, the estimated maximum Re that allows for a developed flow is found to be ~1000. Furthermore, it must be considered that for Re below the onset of turbulence, a transition flow regime is, nevertheless, expected. The analysis of the profiles in the aneurysm evidences a retrograde flow; the magnitude of the peak (negative) retrograde velocity is found to increase with Re. Noticeably, the profiles in the healthy aorta and in the aneurysm almost overlap for the highest Re values.

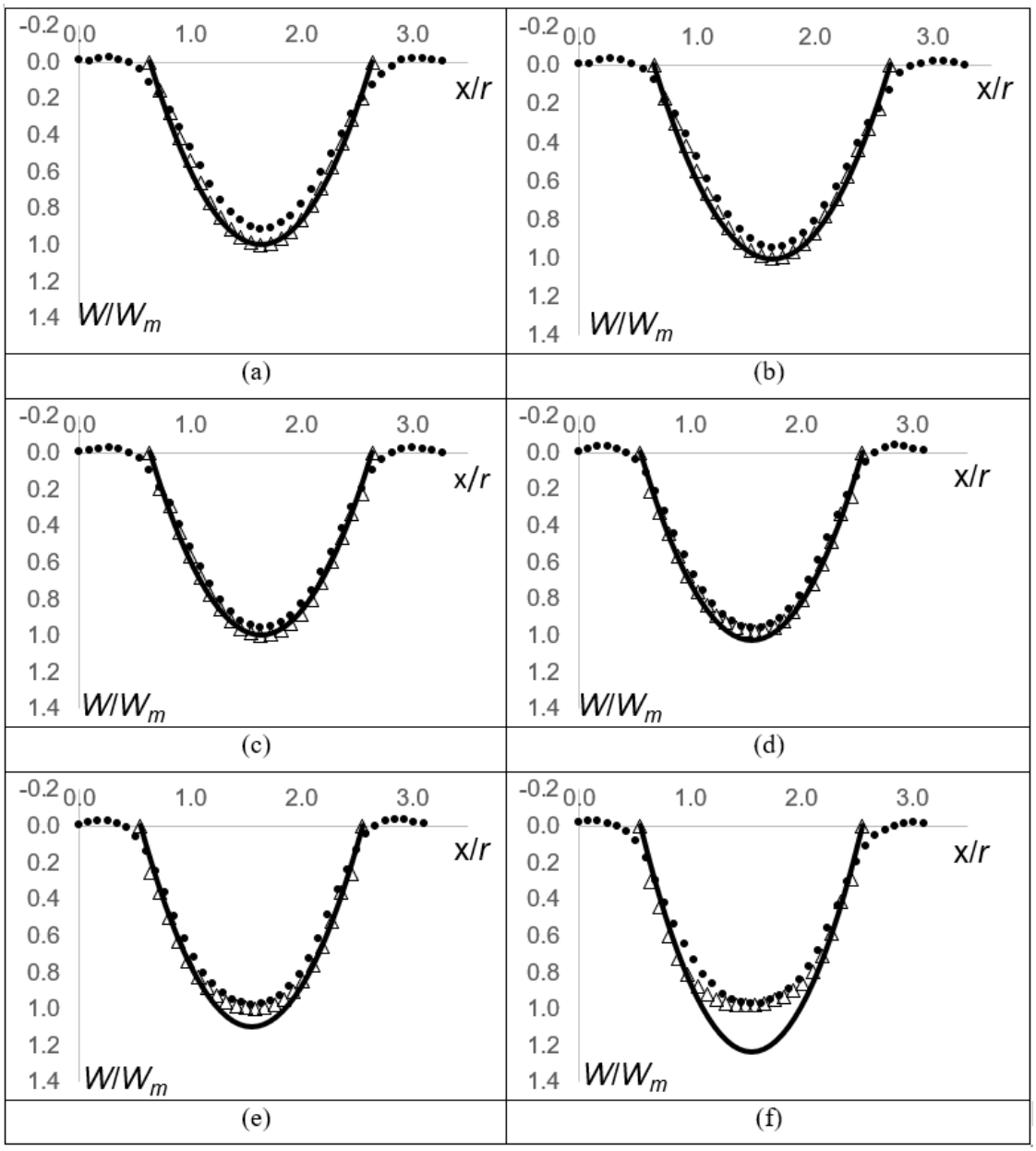

Figure 4. Normalized velocity profiles in correspondence of the maximum vessel diameter for various selected *Re*: (**a**) *Re* = 410, (**b**) *Re* = 600, (**c**) *Re* = 1100, (**d**) *Re* = 1600, (**e**) *Re* = 2000, and (**f**) *Re* = 2650. Data are from the first set of experiments (ID 1 to 6, Table 1). The profiles refer to the healthy aorta (triangles), the aneurysmatic dilatation (circles) and the analytical Poiseuille profile (black continuous line); the x axis is normalized by the radius of the healthy aorta, *r*. Flow direction is from up to down.

Figure 5 shows the streamlines and the distribution of the longitudinal velocity *W* calculated for the average flow field at various *Re*. Basically, the flow pattern consists in a main flow channel with associated zones of low-velocity recirculation corresponding to flow detachment at the model inlet and reattachment at its distal end; as known, flow detachment is associated with positive pressure gradients.

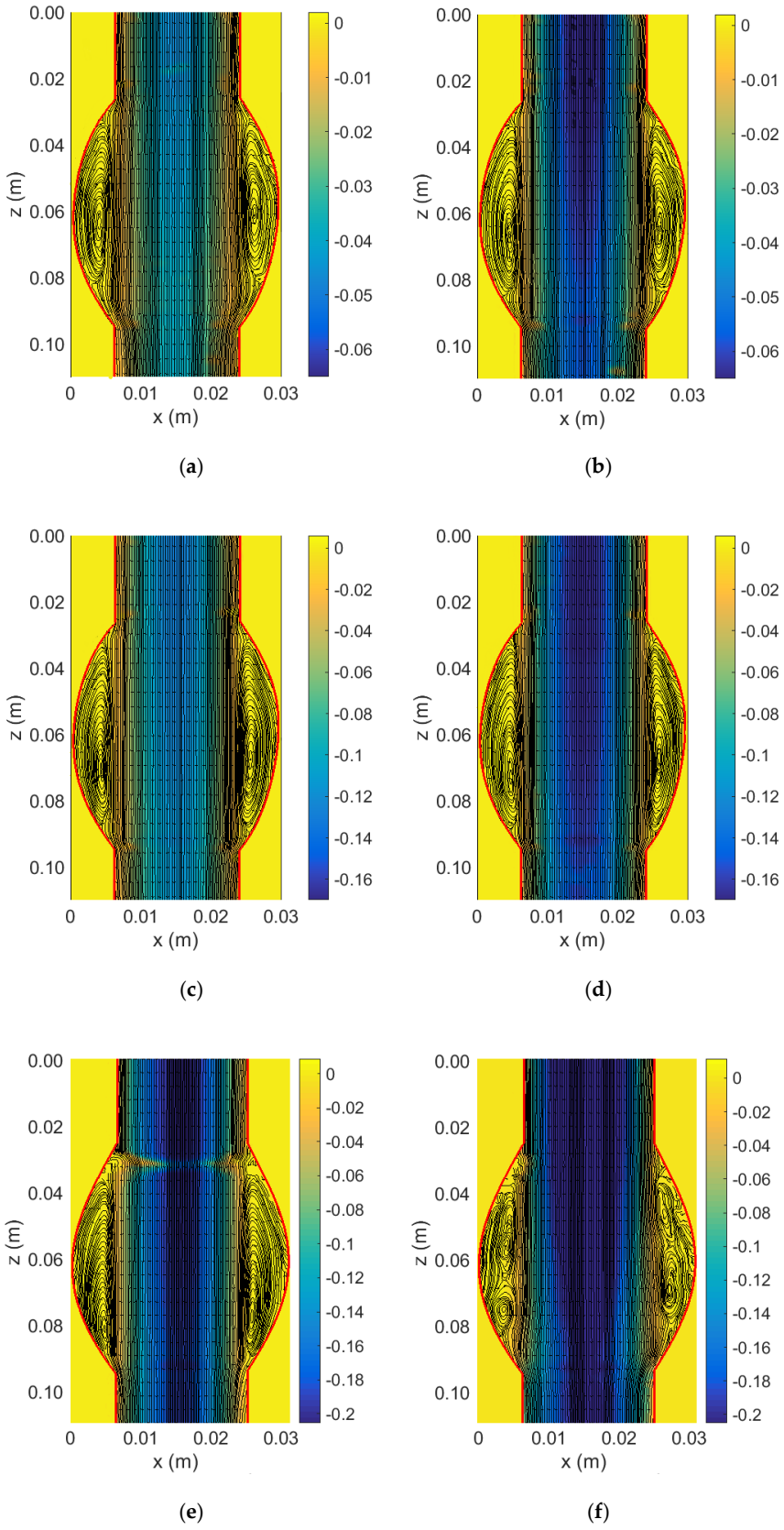

Figure 5. Streamlines and longitudinal velocity (m/s) distribution of the average flow field for the selected *Re*: (**a**) *Re* = 410, (**b**) *Re* = 600, (**c**) *Re* = 1100, (**d**) *Re* = 1600, (**e**) *Re* = 2000, and (**f**) *Re* = 2650. Data are from the second set of experiments (ID 1′ to 6′, Table 1).

As a matter of fact, this region is believed to be a probable site of aneurysm rupture; nevertheless, the role of low WSS has to be taken into account to fully characterize the rupture event [14].

A vortex pattern characterized by retrograde flow with respect to the main flow channel lies in the recirculation zones. The motion of the fluid particles can be better visualized in the movies uploaded as Supplementary Materials showing the time evolution of the reconstructed particles trajectories for the runs at Re = 1100, 2650. In the bulge, particles are shown to follow elliptical type trajectories; as shown by several authors, i.e., in [9,19,20]. In analogous conditions, the center of the recirculation regions moves downstream toward the distal end of the aneurysm, and this displacement is found to increase with Re. We have recovered an analogous behavior. Also, it must be noted that for increasing Re, the flow tends to become unstable: several eddies form in the bulge, and their edges appear to be irregular. This behavior is clearly visible in the uploaded movies (movie_Re1100.avi, movie_Re2650.avi).

WSS in a vessel is the tangential force per unit area acted by the blood flow and is, by definition, calculated as the product of the spatial gradient of the velocity component normal to the wall and the fluid viscosity (see the Appendix A for further details). Normalized WSSs τ_{wn} for varying Re are shown in Figure 6; the normalization is obtained considering the WSS of the healthy aorta τ_h, i.e., $\tau_{wn} = \tau_w/\tau_h$, where τ_w is the WSS.

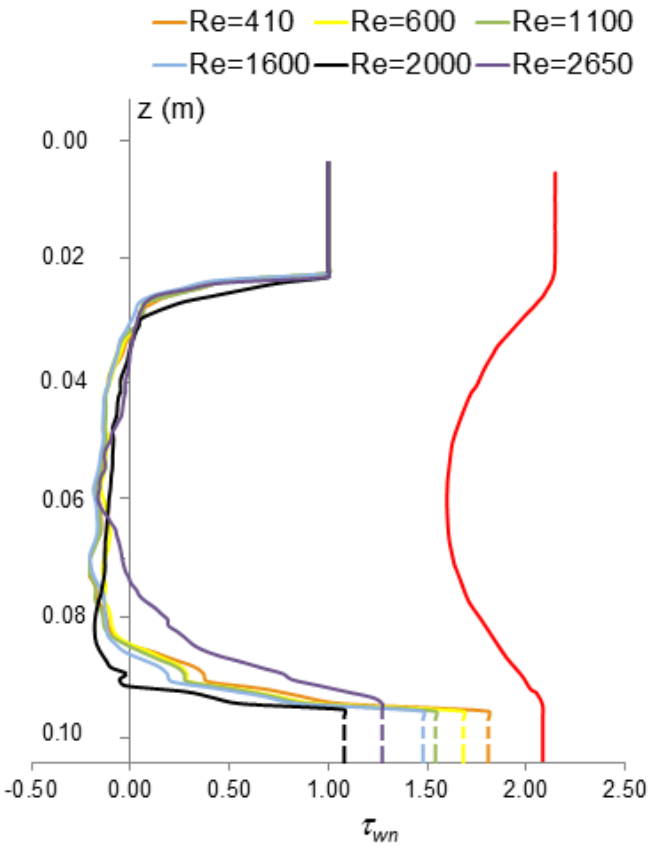

Figure 6. Normalized wall shear stress (WSS) τ_{wn} for varying Re. The red line represents the left aorta boundary. Data are from the second set of experiments (ID 1′ to 6′, Table 1).

For all the examined Re, the recovered trend shows that the WSS values rapidly approach zero in correspondence of the proximal neck, i.e., around the detachment point, and maintain a near zero value in the aneurysmal cavity; a sharp peak occurs in correspondence of the reattachment point. A decrease of the WSS is expected after the peak values, but we were not able to recover it since the framed area in the performed measurements did not extend to a long enough portion of the aorta downstream of the bulge. In Figure 6, the dashed lines have then to be considered as representative of the WSS recovered just in correspondence of the distal neck. The peak value is found to decrease with Re and to be about

twice the upstream value; this ratio is in agreement with [20,32], while several authors found a greater value [19]. As highlighted by several authors, the peak strongly depends on the bulge shape and on the geometry in correspondence of the distal neck [20], as well as on the discretization considered in the numerical scheme [33]. In particular, Patel et al. [20] proved that in the presence of the downstream bifurcation with a stenosed common iliac artery, the time-averaged WSS is lowered with respect to the values observed in a healthy aorta. Moreover in [11,18,19], the authors found very low values of WSS in correspondence of the recirculation zones, a peak in correspondence of the distal neck, as well as a shift towards the exit section of the aneurysm and a reduction of the recirculation zone as the Reynolds number increases.

We remark that the rupture risk, as well as its location, are still debated issues. On the one hand, Boyd et al. [10] have shown that in most cases the rupture does not occur where pressure and WSS are maximal but in recirculation zones where low WSS and ILT deposition predominate and in areas of reduced flow velocity; on the other hand, elevated wall stress seems to be associated with rupture events [34]. Additionally, in [9] the authors emphasized how the spatial distribution of the WSSG may be considered as a hemodynamic force causing damage to the arterial wall at an intermediate stage of growth of the aneurysm.

4. Conclusions

An in-vitro study of a fusiform AAA was performed using image analysis. We were able to recover the flow patterns observed in correspondence of both the healthy vessel and the aneurysm and to investigate the WSS distribution for varying *Re*. In particular, the recirculation zone, which is known to play a fundamental role in the deposition events associated with aneurysms, is found to move downstream, and this displacement is found to increase with *Re*. Results show very low values of WSS in correspondence of the aneurysmal cavity and a sharp peak in correspondence of the reattachment point. The peak value is found to decrease with Re and to equal about twice the upstream value.

Compared to PIV, the particle tracking technique allows for a larger spatial resolution and an increased dynamic range as it is able to detect regions very close to the walls [29]. We believe that this aspect makes HLPT particularly suited for the computation of WSS in this context. Moreover, when WSS is estimated in in-vitro models through velocity measurements, ambiguities in the velocity vectors detection may arise close to the wall due to the light scattering in correspondence of the liquid–solid interface. We were able to avoid this issue via a proper design of the test section.

This study is to be considered as a preliminary stage for the realization of an in-vitro physiological model, including both the wall elasticity and flow time variability, suitable to investigate the correlation of the local hemodynamic characteristics (velocity and vorticity distributions, pressure and wall shear stress fields, transport topology, turbulence) with the abdominal aortic aneurysm progression and the rupture location. In perspective, the particle trajectories provided as an output by this technique may prove particularly suited to investigate blood cell transport [35] and to quantify these phenomena using a Lagrangian approach [32].

Supplementary Materials: The velocity data used to support the findings of this study are available from the corresponding author upon request. The following are available online at http://www.mdpi.com/2076-3417/9/21/4560/s1, Video S1: movie_Re1100.avi, Video S2: movie_Re2650.avi.

Author Contributions: conceptualization, S.E., M.M. and M.A.B.; data curation, M.M.; funding acquisition, S.E. and M.A.B.; investigation, S.E. and M.M.; methodology, S.E., M.M. and M.A.B.; writing—original draft, S.E., M.M. and M.A.B.; writing—review and editing, S.E. and M.M.

Funding: The financial support provided by Sapienza University of Rome research projects (Grant n. RP116155033CC02F and RM11816436229621) is gratefully acknowledged.

Acknowledgments: The authors thank Francesca Patarini and Giorgia Peticca for the useful support provided during the experimental campaign.

Conflicts of Interest: The authors declare no conflict of interest.

List of Symbols

ρ	density of the working fluid (kg m^{-3}) (reference value for pure water: $\rho = 10^3$ kg m^{-3})
μ	dynamic viscosity of the working fluid (N s m^{-2}) (reference value for pure water at 20 °C: $\mu = 10^{-3}$ N s m^{-2})
ν	kinematic viscosity (m^2 s^{-1}) (reference value for pure water at 20 °C: $\nu = 10^{-6}$ m^{2}s^{-1})
τ_h	wall shear stress in the healthy aorta (N m^{-2})
τ_{wn}	normalized wall shear stress
D	maximum inner diameter of the aneurism (cm)
d, r	inner diameter and radius of the healthy aorta (cm)
d_p	tracers particle average diameter (μm)
ρ_p	particle tracers density (kg m^{-3})
L_a	length of the aneurysm (cm)
l_e	entrance length for a straight circular tube (cm)
λ	laser wavelength (μm)
U, W	time-averaged velocity components in the measurement plane (m s^{-1})
W_b	bulk velocity (m s^{-1})
Q	flow rate (m^3 s^{-1})
σ	cross section in correspondence of the healthy aorta (cm^2)
Re	Reynolds number based on the bulk velocity

List of Abbreviations

AAA	Abdominal Aortic Aneurysm
CFD	Computational Fluid Dynamics
HLPT	Hybrid Lagrangian Particle Tracking
ILT	Intra-luminal Thrombus
PIV	Particle Image Velocimetry
PTV	Particle Tracking Velocimetry
PWRR	Peak Wall Rupture Risk
PWSS	Peak Wall Shear Stress
WSS	Wall Shear Stress
WSSG	Wall Shear Stress Gradient

Appendix A

To quantify the WSS on an infinitesimal oriented surface element $d\boldsymbol{S}$ of the wall we considered the total stress τ occurring on it i.e. WSS = $2\ \tau \cdot \boldsymbol{t}$where $\tau = \boldsymbol{Tn}$, $\boldsymbol{T}$ is the stress tensor, for a Newtonian fluid $\boldsymbol{T} = 1/2\ \mu\ [\nabla \boldsymbol{u} + \nabla \boldsymbol{u}^T]$, $\nabla \boldsymbol{u}$ is the velocity gradient tensor ($1/2\ [\nabla \boldsymbol{u} + \nabla \boldsymbol{u}^T]$ represents then the rate of deformation tensor) and $\boldsymbol{n}$ and $\boldsymbol{t}$ are, respectively, the unit vectors normal and tangential to $d\boldsymbol{S}$ [18,20].

Since all quantities need to be evaluated in correspondence of the wall surfaces, we need first to know the equation of its profiles. This equation was obtained through image analysis by following the steps listed below:

- Images of the vessel model (healthy aorta + aneurysmal bulge) were acquired (see Figure A1a).
- Boundaries were reconstructed through image analysis. In particular, by means of a pre-processing procedure (background subtraction), the contrast between the walls and the background was emphasized, a subsequent edge detection allows for the extraction of pixels belonging to the walls.
- The obtained discrete sets of pixels were then interpolated using sixth-order polynomials (see Figure A1b). Considering a 2D acquisition in the x-z plane, an equation $x = f\ (z)$ is then obtained for both right and left wall profiles.

In Figure A1, we reported an example of an acquired image, the reconstructed vessel boundaries, and the image resulting after the application of the mask.

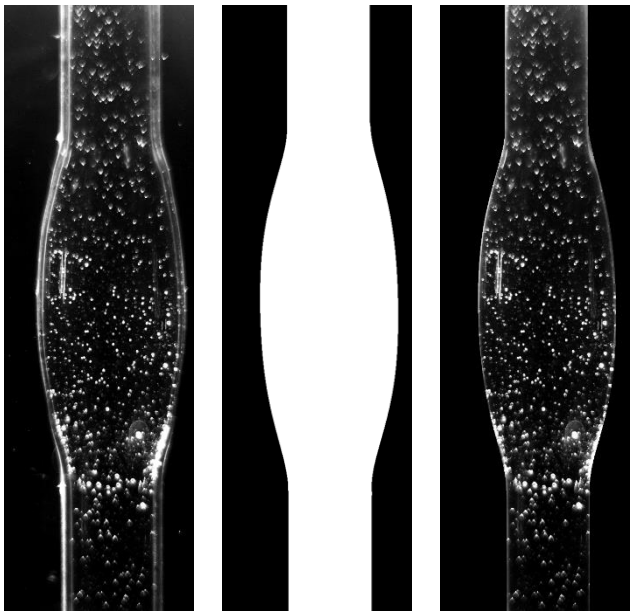

(**a**) (**b**) (**c**)

Figure A1. Example of (**a**) an acquired image, (**b**) the reconstructed vessel boundaries, (**c**) the image resulting after the masking procedure.

As sketched in Figure A2, the first derivative of this function provides the slope of the curve at each point, $dx/dz = f'(z) = tan\theta$ and the x-z components of the unit tangent and normal vectors are found, respectively, as $n_x = cos\theta = t_z$; $n_z = sin\theta = -t_x$.

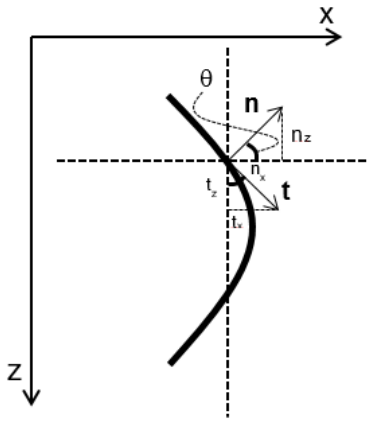

Figure A2. Wall profile and the correspondent local normal-tangent reference frame.

Once the flow field is measured on a plane by means of 2D image analysis, the velocity components u and w are obtained on each point of a 256 x 60 regular grid and the stress tensor can be calculated as:

$$\boldsymbol{T} = \frac{1}{2}\mu\begin{bmatrix} 2\frac{\partial u}{\partial x} & \left(\frac{\partial w}{\partial x} + \frac{\partial u}{\partial z}\right) \\ \left(\frac{\partial u}{\partial z} + \frac{\partial w}{\partial x}\right) & 2\frac{\partial w}{\partial z} \end{bmatrix}; \tag{A1}$$

the WSS is then:

$$\begin{aligned} \text{WSS} = \mu\begin{bmatrix} 2\frac{\partial u}{\partial x} & \left(\frac{\partial w}{\partial x}+\frac{\partial u}{\partial z}\right) \\ \left(\frac{\partial u}{\partial z}+\frac{\partial w}{\partial x}\right) & 2\frac{\partial w}{\partial z} \end{bmatrix}\begin{bmatrix} cos\theta \\ sin\theta \end{bmatrix}\begin{bmatrix} -sin\theta \\ cos\theta \end{bmatrix} = \\ \mu\begin{bmatrix} 2\frac{\partial u}{\partial x} & \left(\frac{\partial w}{\partial x}+\frac{\partial u}{\partial z}\right) \\ \left(\frac{\partial u}{\partial z}+\frac{\partial w}{\partial x}\right) & 2\frac{\partial w}{\partial z} \end{bmatrix}\begin{bmatrix} n_x \\ n_z \end{bmatrix}\begin{bmatrix} -n_z \\ n_x \end{bmatrix} = \mu\left[\left(\frac{\partial w}{\partial x}+\frac{\partial u}{\partial z}\right)\left(n_x^2-n_z^2\right)+2n_xn_z\left(\frac{\partial w}{\partial z}-\frac{\partial u}{\partial x}\right)\right]. \end{aligned} \tag{A2}$$

To give an estimation of the maximum possible shear stress on the surface, one can consider the following expression [36]:

$$WSS_{max} = \frac{\tau_2-\tau_1}{2} = \mu(e_2-e_1) \tag{A3}$$

where τ_i and e_i are, respectively, the eigenvalues of the stress and of the rate-of-deformation tensor. Below, the procedure considered to obtain the expression is shown.

In a principal component reference system, the stress tensor can be written as

$$\boldsymbol{T} = \begin{bmatrix} \tau_1 & 0 \\ 0 & \tau_2 \end{bmatrix} \tag{A4}$$

$$\boldsymbol{T}\cdot\boldsymbol{n} = \begin{bmatrix} \tau_1 & 0 \\ 0 & \tau_2 \end{bmatrix}\begin{bmatrix} cos\theta \\ sin\theta \end{bmatrix} = \begin{bmatrix} \tau_1 cos\theta \\ \tau_2 sin\theta \end{bmatrix} \tag{A5}$$

$$\boldsymbol{T}\cdot\boldsymbol{n}\cdot\boldsymbol{t} = \begin{bmatrix} \tau_1 cos\theta \\ \tau_2 sin\theta \end{bmatrix}\begin{bmatrix} -sin\theta \\ cos\theta \end{bmatrix} = -\tau_1 cos\theta sin\theta + \tau_2 sin\theta cos\theta = \frac{(\tau_2-\tau_1)}{2} sin2\theta \tag{A6}$$

that is maximum at $sin2\theta = 1$ i.e., $\theta = \pi/4$.

References

1. Aggarwal, S.; Qamar, A.; Sharma, V.; Sharma, A. Abdominal aortic aneurysm: A comprehensive review. *Exp. Clin. Cardiol.* **2011**, *16*, 11–15.
2. Hoornweg, L.L.; Storm-Versloot, M.N.; Ubbink, T.; Koelemay, M.J.W.; Legemate, D.A.; Balm, R. Meta analysis on mortality of ruptured abdominal aortic aneurysms. *Eur. J. Vasc. Endovasc. Surg.* **2008**, *35*, 558–570. [CrossRef]
3. Crawford, C.M.; Hurtgen-Grace, K.; Talarico, E.; Marley, J. Abdominal aortic aneurysm: An illustrated narrative review. *J. Manip. Physiol. Ther.* **2003**, *263*, 184–195. [CrossRef]
4. Go, A.S.; Mozaffarian, D.; Roger, V.L.; Benjamin, E.J.; Berry, J.D.; Borden, W.B.; Bravata, D.M.; Dai, S.; Ford, E.S.; Fox, C.S.; et al. Heart disease and stroke statistics—2013 update: A report from the American Heart Association. *Circulation* **2013**, *127*, e6–e245. [CrossRef] [PubMed]
5. Nandlall, S.D.; Goldklang, M.P.; Kalashian, A.; Dangra, N.A.; D'Armiento, J.M.; Konofagou, E.E. Monitoring and staging abdominal aortic aneurysm disease with pulse wave imaging. *Ultrasound Med. Biol.* **2014**, *40*, 2404–2414. [CrossRef]
6. Chaikof, E.L.; Dalman, R.L.; Eskandari, M.K.; Jackson, B.M.; Lee, W.A.; Mansour, M.A.; Mastracci, T.M.; Mell, M.; Murad, M.H.; Nguyen, L.L.; et al. The Society for Vascular Surgery practice guidelines on the care of patients with an abdominal aortic aneurysm. *J. Vasc. Surg.* **2018**, *67*, 2–77. [CrossRef] [PubMed]
7. Heng, M.S.; Fagan, M.J.; Collier, J.W.; Desai, G.; McCollum, P.T.; Chetter, I.C. Peak wall stress measurement in elective and acute abdominal aortic aneurysms. *J. Vasc. Surg.* **2008**, *47*, 17–22. [CrossRef] [PubMed]
8. Gasser, T.C.; Auer, M.; Labruto, F.; Swedenborg, J.; Roy, J. Biomechanical rupture risk assessment of abdominal aortic aneurysms: Model complexity versus predictability of finite element simulations. *Eur. J. Vasc. Endovasc. Surg.* **2010**, *40*, 176–185. [CrossRef] [PubMed]
9. Finol, E.A.; Amon, C.H. Flow-induced wall shear stress in abdominal aortic aneurysms: Part I—Steady flow hemodynamics. *Comput. Methods Biomech. Biomed. Eng.* **2002**, *5*, 309–318. [CrossRef]
10. Li, Z.; Kleinstreuer, C. A comparison between different asymmetric abdominal aortic aneurysm morphologies employing computational fluid-structure interaction analysis. *Eur. J. Mech. B Fluids* **2007**, *26*, 615–631. [CrossRef]

11. Bluestein, D.; Niu, L.; Schoephoerster, R.T.; Dewanjee, M.K. Steady flow in an aneurysm model: Correlation between fluid dynamics and blood platelet deposition. *J. Biomech. Eng.* **1996**, *118*, 280–286. [CrossRef] [PubMed]
12. Zambrano, B.A.; Gharahi, H.; Lim, C.; Jaberi, F.A.; Lee, W.; Baek, S. Association of intraluminal thrombus, hemodynamic forces, and abdominal aortic aneurysm expansion using longitudinal CT images. *Ann. Biomed. Eng.* **2016**, *44*, 1502–1514. [CrossRef] [PubMed]
13. Haller, S.J.; Crawford, J.D.; Courchaine, K.M.; Bohannan, C.J.; Landry, G.J.; Moneta, G.L.; Azarba, A.F.; Rugonyi, S. Intraluminal thrombus is associated with early rupture of abdominal aortic aneurysm. *J. Vasc. Surg.* **2018**, *67*, 1051–1058. [CrossRef] [PubMed]
14. Boyd, A.J.; Kuhn, D.C.S.; Lozowy, R.J.; Kulbisky, G.P. Low wall shear stress predominates at sites of abdominal aortic aneurysm rupture. *J. Vasc. Surg.* **2016**, *47*, 1613–1619. [CrossRef] [PubMed]
15. Querzoli, G.; Fortini, S.; Espa, S.; Costantini, M.; Sorgini, F. Fluid dynamics of aortic root dilation in Marfan syndrome. *J. Biomech.* **2014**, *47*, 3120–3128. [CrossRef] [PubMed]
16. Querzoli, G.; Fortini, S.; Espa, S.; Melchionna, S. A laboratory model of the aortic root flow including the coronary arteries. *Exp. Fluids* **2016**, *57*, 134. [CrossRef]
17. Yazdi, S.G.; Huetter, L.; Docherty, P.D.; Williamson, P.N.; Clucas, D.; Jermy, M.; Geoghegan, P.H. A Novel Fabrication Method for Compliant Silicone Phantoms of Arterial Geometry for Use in Particle Image Velocimetry of Haemodynamics. *Appl. Sci.* **2019**, *9*, 3811. [CrossRef]
18. Salsac, A.V.; Sparks, S.R.; Chomaz, J.M.; Lasheras, J.C. Evolution of the wall shear stresses during the progressive enlargement of symmetric abdominal aortic aneurysms. *J. Fluid Mech.* **2006**, *560*, 19–51. [CrossRef]
19. Stamatopoulos, C.; Papaharilaou, Y.; Mathioulakis, D.S.; Katsamouris, A. Steady and unsteady flow within an axisymmetric tube dilatation. *Exp. Therm. Fluid Sci.* **2010**, *34*, 915–927. [CrossRef]
20. Patel, S.; Abdullah, Y.; Usmani, Y.; Muralidhar, K. Effect of aorto-iliac bifurcation and iliac stenosis on flow dynamics in an abdominal aortic aneurysm. *Fluid Dyn. Res.* **2017**, *49*, 1–29. [CrossRef]
21. Boutsianis, E.; Guala, M.; Olgac, U.; Wildermuth, S.; Hoyer, K.; Ventikos, Y.; Poulikakos, D. CFD and PTV steady flow investigation in an anatomically accurate abdominal aortic aneurysm. *J. Biomech. Eng.* **2009**, *131*(1), 11008. [CrossRef] [PubMed]
22. Stamatopoulos, C.; Mathioulakis, D.S.; Papaharilaou, Y.; Katsamouris, A. Experimental unsteady flow study in a patient-specific abdominal aortic aneurysm model. *Exp. Fluids* **2011**, *50*, 1695–1709. [CrossRef]
23. Soudah, E.; Ng, E.Y.K.; Loong, T.H.; Bordone, M.; Pua, U.; Narayanan, S. CFD Modelling of Abdominal Aortic Aneurysm on Hemodynamic Loads Using a Realistic Geometry with CT. *Comput. Math. Methods Med.* **2013**, *2013*, 472564. [CrossRef] [PubMed]
24. Shindler, L.; Moroni, M.; Cenedese, A. Using optical flow equation for particle detection and velocity prediction in particle tracking. *Appl. Math. Comput.* **2012**, *218*, 8684–8694. [CrossRef]
25. Deplano, V.; Knapp, Y.; Bertrand, E.; Gaillard, E. Flow behaviour in an asymmetric compliant experimental model for abdominal aortic aneurysm. *J. Biomech.* **2007**, *40*, 2406–2413. [CrossRef] [PubMed]
26. Khanafer, K.M.; Bull, J.L.; Berguer, R. Fluid–structure interaction of turbulent pulsatile flow within a flexible wall axisymmetric aortic aneurysm model. *Eur. J. Mech. B Fluids* **2009**, *28*, 88–102. [CrossRef]
27. Ene, F.; Delassus, P.; Morris, L. The influence of computational assumptions on analyzing abdominal aortic aneurysm haemodynamics. *Proc. Inst. Mech. Eng. Part H J. Eng. Med.* **2014**, *228*, 768–780. [CrossRef]
28. Usmani, A.Y.; Muralidhar, K. Pulsatile flow in a compliant stenosed asymmetric model. *Exp. Fluids* **2016**, *57*, 1–24. [CrossRef]
29. Moroni, M.; Cenedese, A. Comparison among feature tracking and more consolidated velocimetry image analysis techniques in a fully developed turbulent channel flow. *Meas. Sci. Technol.* **2005**, *16*, 2307–2322. [CrossRef]
30. Moroni, M.; Giorgilli, M.; Cenedese, A. Experimental investigation of slope flows via image analysis techniques. *J. Atmos. Sol. Terr. Phys.* **2014**, *108*, 17–33. [CrossRef]
31. Shah, R.K.; Bhatti, M.S. Laminar convective heat transfer in ducts. In *Handbook of Single-Phase Connective Heat Transfer*; Wiley: New York, NY, USA, 1987.
32. Choudhury, S.; Anupindi, K.; Patnaik, B.S.V. Influence of wall shear stress and geometry on the lumen surface concentration of low density lipoprotein in a model abdominal aortic aneurysm. *Phys. Fluids* **2019**, *31*, 1–13. [CrossRef]

33. Febina, J.; Sikkandar, M.Y.; Sudharsan, N.M. Wall Shear Stress Estimation of Thoracic Aortic Aneurysm Using Computational Fluid Dynamics. *Comput. Math. Methods Med.* **2018**, *2018*, 7126532. [CrossRef] [PubMed]
34. Fillinger, M.F.; Marra, S.P.; Raghavan, M.L.; Kennedy, F.E. Prediction of rupture risk in abdominal aortic aneurysm during observation: Wall stress versus diameter. *J. Vasc. Surg.* **2003**, *37*, 724–773. [CrossRef] [PubMed]
35. Wu, W.-T.; Li, Y.; Aubry, N.; Massoudi, M.; Antaki, J.F. Numerical Simulation of Red Blood Cell-Induced Platelet Transport in Saccular Aneurysms. *Appl. Sci.* **2017**, *7*, 484. [CrossRef]
36. Cenedese, A.; Del Prete, Z.; Miozzi, M.; Querzoli, G. A laboratory investigation of the flow in the left ventricle of the human heart with prosthetic, tilting-disk valves. *Exp. Fluids* **2005**, *39*, 322–335. [CrossRef]